

## Flat-Band Potentials of Molecularly Thin Metal Oxide Nanosheets

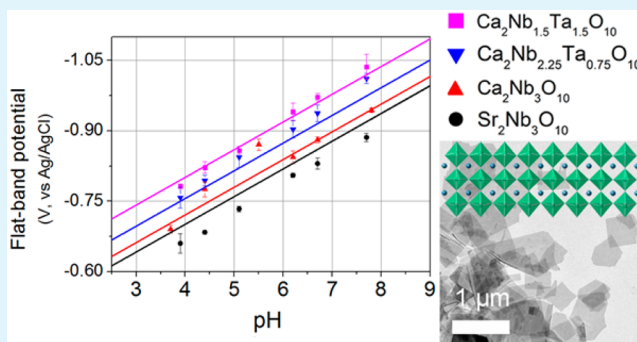
Pengtao Xu, Tyler J. Milstein, and Thomas E. Mallouk\*

Departments of Chemistry, Physics, and Biochemistry and Molecular Biology, The Pennsylvania State University, University Park, Pennsylvania 16802, United States

## Supporting Information

**ABSTRACT:** Exfoliated nanosheets derived from Dion–Jacobson phase layer perovskites ( $\text{TBA}_x\text{H}_{1-x}\text{A}_2\text{B}_3\text{O}_{10}$ , A = Sr, Ca, B = Nb, Ta) were grown layer-by-layer on fluorine-doped tin oxide and gold electrode surfaces. Electrochemical impedance spectra (EIS) of the five-layer nanosheet films in contact with aqueous electrolyte solutions were analyzed by the Mott–Schottky method to obtain flat-band potentials ( $V_{\text{FB}}$ ) of the oxide semiconductors as a function of pH. Despite capacitive contributions from the electrode–solution interface, reliable values could be obtained from capacitance measurements over a limited potential range near  $V_{\text{FB}}$ . The measured values of  $V_{\text{FB}}$  shifted  $-59$  mV/pH over the pH range of 4–8 and were in close agreement with the empirical correlation between conduction band-edge potentials and optical band gaps proposed by Matsumoto (*J. Solid State Chem.* **1996**, *126* (2), 227–234). Density functional theory calculations showed that A-site substitution influenced band energies by modulating the strength of A–O bonding, and that substitution of Ta for Nb on B-sites resulted in a negative shift of the conduction band-edge potential.

**KEYWORDS:** layered metal oxide, semiconductor, nanosheets, flat-band potential, water splitting, perovskite



## INTRODUCTION

Nanosheets that are made by intercalation and exfoliation of layered metal oxides are two-dimensional crystals, which are used as building blocks of materials that exploit their electronic, magnetic, dielectric, optical, catalytic, and ion-exchange properties.<sup>1,2</sup> Metal oxide nanosheets that contain  $d^0$  transition metal ions such as  $\text{Ti}^{4+}$ ,  $\text{Nb}^{5+}$ , and  $\text{Ta}^{5+}$  have been of special interest as light absorbers, electron acceptors, and electron transfer mediators in solar photochemical applications.<sup>3</sup> Domen and co-workers introduced the photochemistry of these materials 30 years ago, showing that layered niobates intercalated with transition metal catalysts could generate hydrogen photochemically from aqueous methanol solutions,<sup>4</sup> and split water when excited with UV light.<sup>5</sup> Layered metal oxides intercalated with transition metal catalysts and photosensitized with dye molecules were later shown to photolyze  $\text{HI}$  to hydrogen and  $\text{I}_3^-$  in visible light.<sup>6–8</sup> The development of techniques for growing nanosheets layer-by-layer on surfaces,<sup>9,10</sup> and for making scrolls and other kinds of structured nanosheet colloids,<sup>11,12</sup> has enabled the study of more complex molecule–nanosheet photochemical assemblies.<sup>13–21</sup> In these cases, the nanosheets mediate electron transfer reactions between electron donors and acceptors, and the quantum yield for productive photochemistry represents a kinetic competition between forward and back electron transfer reactions. It is thus of paramount importance to control these rates, which in turn requires knowledge of the energetics of the electron transfer reactions. While it is straightforward to

measure the bandgaps of oxide semiconductors (either in bulk form or as exfoliated nanosheets) by optical methods, the band-edge potentials, which determine the driving forces of electron transfer reactions, have been more challenging to measure directly.

Metal oxide nanosheets such as titanates, niobates, and tantalates are typically  $n$ -type semiconductors in which Fermi level ( $E_{\text{F}}$ ) is located close to conduction band minimum. In (photo)electrochemistry,  $E_{\text{F}}$  is equivalent to the flat-band potential ( $V_{\text{FB}}$ ) when band bending at the semiconductor surface disappears.<sup>22</sup> Two methods are typically used to characterize  $V_{\text{FB}}$  of semiconductors in solution, the photocurrent-onset potential method and the Mott–Schottky method.<sup>23</sup> Using the first method, Sakai et al.<sup>24</sup> and Akatsuka et al.<sup>25</sup> characterized  $V_{\text{FB}}$  of representative titanate and niobate nanosheets in  $\text{LiClO}_4$ /propylene carbonate solutions. These measurements, unfortunately, do not give  $V_{\text{FB}}$  of the nanosheets under aqueous conditions, because in nonaqueous solvents  $V_{\text{FB}}$  can be affected by the type of supporting salts and their concentrations.<sup>26</sup> Chamousis et al.<sup>27</sup> conducted photocurrent-onset potential measurements in methanol to determine  $V_{\text{FB}}$  of calcium niobate nanosheets restacked from different solutions, demonstrating that specific ion adsorption can affect the energetics of the nanosheets (and hence their

Received: March 8, 2016

Accepted: April 22, 2016

Published: April 22, 2016

photocatalytic activities). So far, no systematic study of the flat-band potentials of single- or few-layer metal oxide nanosheets in aqueous solutions has been reported. The challenge for photocurrent measurements in aqueous solutions arises from the fact that the nanosheets are wide band gap oxides that absorb only UV light, and kinetic barriers for catalytic photoreactions can shift the photocurrent onset away from  $V_{\text{FB}}$  (typically in the anodic direction for n-type materials).<sup>23</sup>

$V_{\text{FB}}$  values for metal oxide nanosheets have been estimated by using empirical rules developed for three-dimensionally bonded oxide semiconductors. An early study by Butler and Ginley developed a correlation based on band gap energies and the average electronegativities of constituent elements to estimate  $V_{\text{FB}}$  values of metal oxide semiconductors.<sup>28</sup> Later, by correlating the band-edge potentials and band gaps of a large number of oxide semiconductors, Matsumoto<sup>29</sup> proposed the empirical correlation between conduction band-edge potentials ( $E_{\text{CB}}$ ) and band gap energies ( $E_{\text{g}}$ ) of a metal oxide semiconductor given in eq 1:

$$E_{\text{CB}} \text{ (V vs RHE)} = 1.23 - \frac{E_{\text{g}} \text{ (eV)}}{2} \quad (1)$$

Although this equation has been widely used to estimate the  $V_{\text{FB}}$  of metal oxide nanosheets,<sup>17,30,31</sup> its reliability for molecularly thin nanosheets is unknown because it was derived from data on bulk, three-dimensionally bonded oxide semiconductors.

The other method used to characterize the  $V_{\text{FB}}$  of semiconductors in contact with solutions is the Mott–Schottky method, which relates the differential capacity of the space charge layer to the applied potential. This method has been widely used for bulk as well as thin film semiconductors.<sup>22,32–34</sup> Recently, Maeda and co-workers reported band-edge tunable perovskite nanosheets of  $\text{HCa}_x\text{Sr}_{2-x}\text{Nb}_y\text{Ta}_{3-y}\text{O}_{10}$  and explored how the band-edge potential influenced their photocatalytic properties.<sup>30,35</sup> Here, we apply the Mott–Schottky method to measure  $V_{\text{FB}}$  of few-layer nanosheets of these materials in contact with aqueous solutions as a function of pH. From these measurements, we can observe a quantitative correlation between the composition of the nanosheets and  $V_{\text{FB}}$ . We also used first-principles electronic structure calculations based on density functional theory (DFT) to correlate the composition of the nanosheets with their corresponding band diagrams.

## EXPERIMENTAL SECTION

**Preparation of Layered Metal Oxide Nanosheets.** Calcium niobate nanosheets ( $\text{TBA}_{1-x}\text{H}_x\text{Ca}_2\text{Nb}_3\text{O}_{10}$ , TBA = tetra(*n*-butylammonium)) and strontium niobate nanosheets ( $\text{TBA}_{1-x}\text{H}_x\text{Sr}_2\text{Nb}_3\text{O}_{10}$ ) were prepared as previously described.<sup>36,37</sup> Briefly, the layered metal oxides  $\text{KCa}_2\text{Nb}_3\text{O}_{10}$  and  $\text{CsSr}_2\text{Nb}_3\text{O}_{10}$  were synthesized by calcining a mixture of  $\text{K}_2\text{CO}_3$  (99%, Alfa Aesar),  $\text{Sr}_2\text{CO}_3$  (99.9%, Aldrich),  $\text{CaCO}_3$  (99.95%, Sigma-Aldrich), and  $\text{Nb}_2\text{O}_5$  (99.99%, Sigma-Aldrich) with elemental ratios K:Ca:Nb = 1.05:2:3 and Cs:Sr:Nb = 1.2:2:3 at 1373 K for 12 h in air. An excess of the alkali metal carbonate was used to compensate for the volatilization at high temperature. The obtained powders were treated with 2 M HCl aqueous solution for 3 days to replace the alkali ions with protons. The proton-exchanged materials were then dispersed in 100 mL of an aqueous solution that contained an equimolar amount of tetra(*n*-butylammonium) hydroxide (TBAOH, prepared from a 40% solution in water, Fluka) and were shaken for at least 1 week at ambient temperature. The nanosheet suspensions were collected after the removal of the unexfoliated particles by centrifugation. In the case of  $\text{TBA}_{1-x}\text{H}_x\text{Ca}_2\text{Nb}_3\text{O}_{10}$  nanosheets, the layered oxides

$\text{RbCa}_2\text{Nb}_3\text{O}_{10}$  were prepared by the polymerized complex method reported by Maeda et al.<sup>35</sup> Nanosheets with *x* values of 2.25 and 1.5 were prepared. In a typical synthesis,  $\text{NbCl}_5$  (99+%, Strem Chemicals, Inc.) and  $\text{TaCl}_5$  (99.99%, Acros Organics) powders were dissolved in 100 mL of methanol with stirring, followed by the addition of  $\text{CaCO}_3$ ,  $\text{RbCl}$  (99%, Alfa Aesar), citric acid (CA, anhydrous, 99.5%, Alfa Aesar), and ethylene glycol (EG, 99+%, Sigma). The molar ratio of  $\text{Rb/Ca}/(\text{Nb+Ta})/\text{Ca/EG}$  was 1.4/2/3/30/120. The solution was then heated to about 65 °C to allow the solvent to evaporate. The esterification reaction between EG and CA was promoted by heating the mixture to about 130 °C, which yielded a slightly brown glassy resin after 1 h. Pyrolysis of the resin was conducted in air at 450 °C for 1 h to produce black powders, which were then heated in an alumina crucible at 600 °C for 4 h in air. The obtained white powders underwent a final calcination in air at 1100 °C for 12 h. The subsequent acid-exchange and exfoliation processes were carried out in a similar fashion to  $\text{KCa}_2\text{Nb}_3\text{O}_{10}$  and  $\text{CsSr}_2\text{Nb}_3\text{O}_{10}$ .

**Layer-by-Layer (LBL) Assembly of the Nanosheets.** Substrates, including fluorine-doped tin oxide-coated glass (FTO, 8 Ω/cm<sup>2</sup>, Hartford Glass Company), quartz (Chemglass Life Sciences), silicon wafers (University Wafer), and gold-coated glass slides (Deposition Research Lab Inc.) were cleaned by sonication in soapy water, isopropyl alcohol, and Nanopure water (each for 10 min), respectively. Poly(diallyldimethylammonium chloride) solution (2 wt %) (PDDA,  $M_w = 1-2 \times 10^5$ , 20 wt % in water, Aldrich) and a diluted nanosheet suspension (~0.5 mg/mL) were prepared for LBL assembly. The clean substrate was first immersed in PDDA solution for 20 min to anchor the positively charged polymer and was then thoroughly rinsed with water and dried in a compressed air stream before being immersed in the nanosheet solution for another 20 min to produce a PDDA/nanosheet bilayer. The deposition was repeated *n* times to construct *n* layers of PDDA/nanosheets.

**Electrochemical Measurements.** Electrochemical measurements were carried out in a three-electrode cell with Ag/AgCl (3.0 M NaCl, +0.210 V vs NHE) as the reference electrode and Pt gauze (100 mesh, 1 × 2 cm<sup>2</sup>) as the counter electrode. Working electrodes were prepared by depositing five layers of nanosheets onto clean FTO-glass and gold-coated slides using the LBL technique described above. Prior to the electrochemical measurements, the electrodes were heated at 200 °C for 30 min to remove solvent and then exposed to UV irradiation (Black-Ray B100-AP lamp, UVP, LLC) for about 3 days to decompose polycations, exploiting the photocatalytic property of the nanosheets. Aqueous 0.1 M KCl containing 10 mM acetate buffer for pH 3 to 6, or 10 mM phosphate buffer for pH 6 to 8, was used as the electrolyte. Accurate pH values were determined by using a pH meter (VWR sympHony SP70P). The electrolyte was purged with nitrogen for 15 min prior to each set of measurements. Electrochemical impedance spectroscopy (EIS) was conducted using Autolab potentiostat with a FRA32 M module. A frequency range of 10<sup>-1</sup>–10<sup>4</sup> Hz and an amplitude of 10 mV were used. EIS measurements at each pH for every material were repeated three times with three different samples to avoid artifacts arising from electrode polarization. All electrode potential values are given with respect to the Ag/AgCl reference electrode unless otherwise noted.

**Characterization.** Samples were characterized by X-ray powder diffraction (XRD, PANalytical Empyrean, Cu Kα radiation), transmission electron microscopy (TEM, JEOL 1200 EXII, accelerating voltage 80 kV), field-emission scanning electron microscopy (FESEM, FEI NanoSEM 630, accelerating voltage 10 kV), and atomic force microscopy (AFM, Bruker Icon microscope, PeakForce Tapping mode). Ultraviolet–visible (UV–vis) absorption spectra of the nanosheets were collected using a Varian Cary 6000i spectrophotometer.

**Electronic Structure Calculations.** All calculations were performed within the framework of DFT as implemented in CASTEP.<sup>38</sup> The structure of a  $\text{HCa}_2\text{Nb}_3\text{O}_{10}$  monolayer was created as reported elsewhere.<sup>39</sup> Initial structures of  $\text{HCa}_2\text{Ta}_3\text{O}_{10}$  and  $\text{HSr}_2\text{Nb}_3\text{O}_{10}$  monolayers were generated by replacing metal ions at the corresponding sites in the  $\text{HCa}_2\text{Nb}_3\text{O}_{10}$  structure. For geometry optimization, the general gradient approximation (GGA) in the

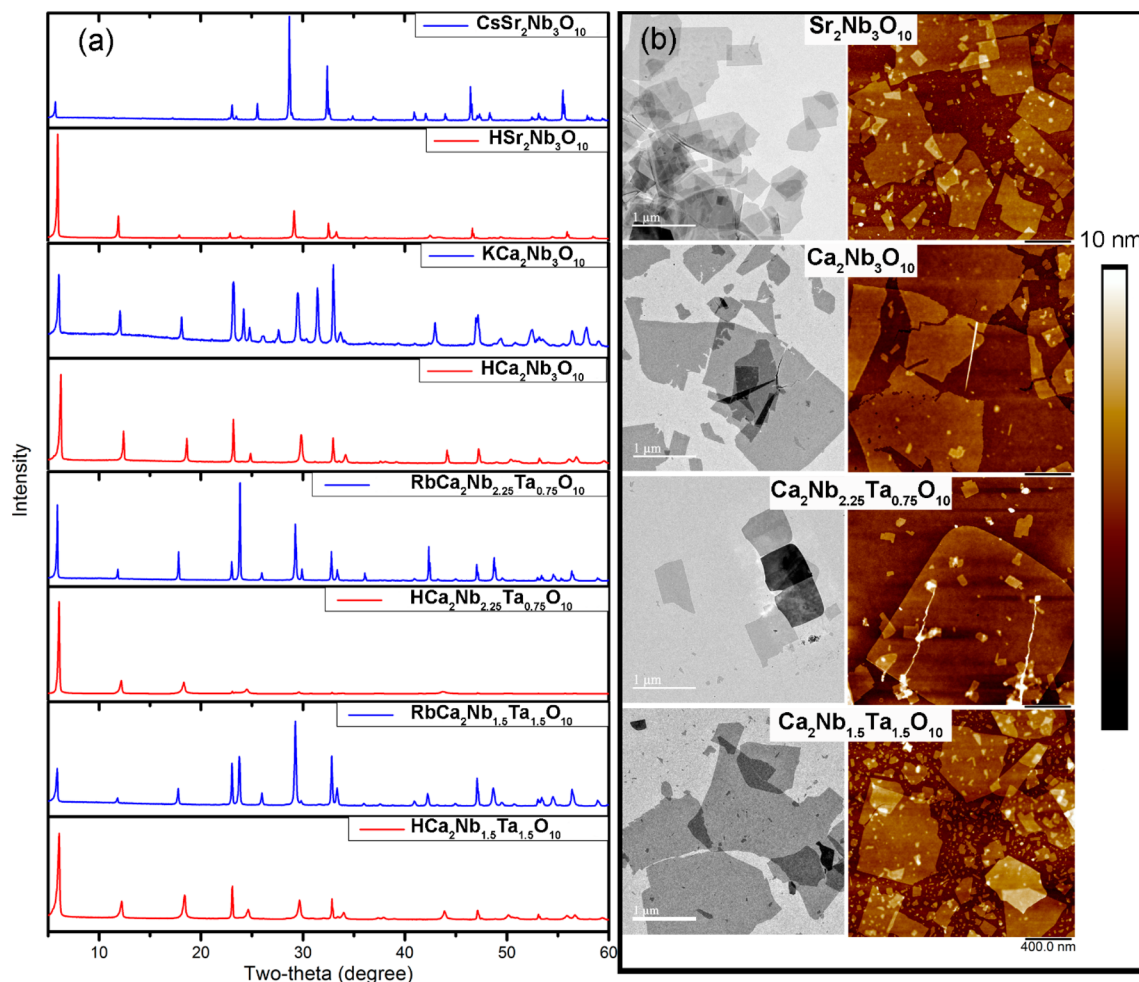


**Figure 1.** (a) XRD patterns of as-prepared layer perovskites and their corresponding proton-exchanged products. (b) TEM (left) and AFM (right) images of the exfoliated nanosheets.

Perdew–Burke–Ernzerhof (PBE) form<sup>40</sup> and a cutoff energy of 400 eV for the plane-wave basis set were employed with a convergence threshold of  $2.0 \times 10^{-5}$  eV/atom for energy and 0.05 eV/Å for force. Integration over the Brillouin zone was performed by using a Monkhorst–Pack (MP) grid of  $2 \times 2 \times 1$ . The work function was determined as the potential difference between the vacuum level and the Fermi level. Bond orders were analyzed using the Mulliken method.<sup>41</sup> For electronic structure calculations, we used the hybrid functional HSE06<sup>42</sup> with a cutoff energy of 800 eV. Band structures were generated along the following high-symmetry points in  $k$ -space with a spacing of 0.08/Å:  $G$  (0, 0, 0),  $F$  (0, 0.5, 0), and  $B$  (0.5, 0, 0). The partial density of states (PDOS) was calculated with a MP grid of  $5 \times 5 \times 1$ .

## RESULTS AND DISCUSSION

**Preparation of Nanosheets.** The layered metal oxides examined in this study belong to the Dion–Jacobson (D–J) structural family of layer perovskites with a general formula of  $A'A_{n-1}B_nO_{3n-1}$ .<sup>43</sup>  $A'$  is an alkali metal cation that separates  $A_{n-1}B_nO_{3n-1}$  perovskite blocks, in which the A cations occupy cubooctahedral sites surrounded by eight corner-sharing  $\text{BO}_6$  octahedra and  $n$  denotes the number of  $\text{BO}_6$  repeat units along the stacking axis in each block. When the parent solids are exfoliated into nanosheets, the  $A'$  cations are replaced by protons and  $\text{TBA}^+$  cations to preserve neutrality. In subsequent discussion, we denote the  $n = 3$   $\text{TBA}_{1-x}\text{H}_x\text{A}_2\text{B}_3\text{O}_{10}$  nanosheets by the shorthand notation  $\text{A}_2\text{B}_3\text{O}_{10}$ . XRD patterns (Figure 1a)

confirmed the successful synthesis of the layered perovskites as well as the proton-exchanged products. TEM images (Figure 1b, left) show that the proton-exchanged products are delaminated into nanosheets. Energy-dispersive X-ray spectroscopy (EDS) was used to determine the compositions of  $\text{Ca}_2\text{Nb}_x\text{Ta}_{3-x}\text{O}_{10}$  nanosheets (Table S1, Supporting Information) and showed that the experimental Nb:Ta ratios for  $\text{Ca}_2\text{Nb}_{2.25}\text{Ta}_{0.75}\text{O}_{10}$  and  $\text{Ca}_2\text{Nb}_{1.5}\text{Ta}_{1.5}\text{O}_{10}$  nanosheets were very close to the 3:1 and 1:1 target ratios, respectively. These nanosheets were further found by AFM to form patchy monolayers in the first step of LBL assembly on Si substrates, despite the presence of a small fraction of multilayer nanoparticles (Figure 1b, right). The thicknesses of the monolayer nanosheets were measured at the edges where the sheets overlapped in order to avoid different tip interaction forces between the substrate and nanosheets. Based on the average five measurements, the thicknesses of the nanosheets were as follows:  $\text{Sr}_2\text{Nb}_3\text{O}_{10}$ ,  $1.73 \pm 0.16$  nm;  $\text{Ca}_2\text{Nb}_3\text{O}_{10}$ ,  $1.60 \pm 0.07$  nm;  $\text{Ca}_2\text{Nb}_{2.25}\text{Ta}_{0.75}\text{O}_{10}$ ,  $1.79 \pm 0.06$  nm;  $\text{Ca}_2\text{Nb}_{1.5}\text{Ta}_{1.5}\text{O}_{10}$ ,  $1.78 \pm 0.07$  nm.

**Layer-by-Layer Assembly.** Exfoliated nanosheets were assembled onto different substrates by sequential adsorption of PDDA and nanosheet solutions.<sup>44</sup> Layer-by-layer assembly of nanosheets on quartz was monitored by UV–vis spectroscopy (Figure 2). The linear growth of the absorbance at 265 nm with increasing layer number indicates that approximately the same

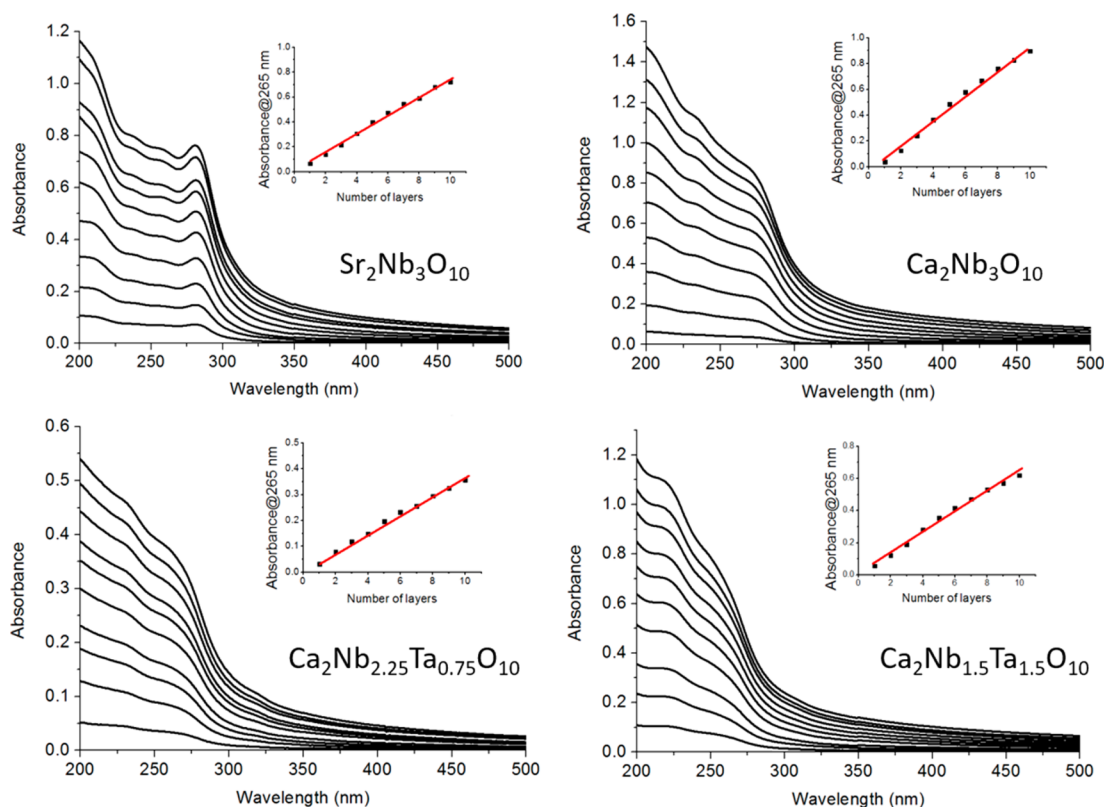


Figure 2. UV-vis absorption spectra of nanosheet multilayers deposited on quartz substrates.

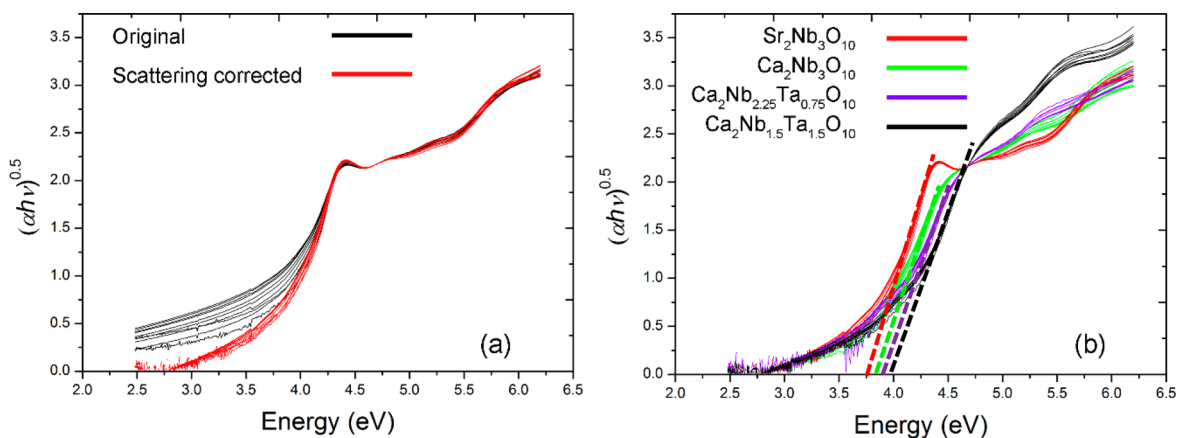


Figure 3. (a) Original and scattering-corrected Tauc plots for one- to ten-layer films of  $\text{Sr}_2\text{Nb}_3\text{O}_{10}$  nanosheets. (b) Scattering-corrected Tauc plots for one- to ten-layer films of nanosheets of different compositions.

amount of nanosheets was deposited in each adsorption cycle. Note that the background absorption ( $\lambda > 350$  nm) also increased with layer number due to Rayleigh scattering from the nanosheets and unexfoliated particles.

**Band Gap Determination.** The optical band gaps ( $E_g$ ) of the nanosheets were determined by converting their UV-vis absorbance spectra into Tauc plots using eq 2:

$$(\hbar\nu\alpha)^{1/n} = A(\hbar\nu - E_g) \quad (2)$$

where  $\hbar$  is Planck's constant,  $\nu$  is the frequency,  $\alpha$  is the absorption coefficient, and  $A$  is a proportionality constant. The exponent  $n$  denotes the nature of photon absorption, where  $n = 1/2$  and  $n = 2$  are used for direct and indirect band gaps, respectively. A linear fit from the point where  $(\hbar\nu\alpha)^{1/n}$  begins

to increase linearly with  $\hbar\nu$  intercepts  $E_g$  on the  $\hbar\nu$  axis. The absorption coefficients of nanosheets used in eq 2 were taken as proportional to the absorbance values at 265 nm, because at this wavelength only the nanosheets, not PDDA nor TBA ions, show strong light absorption. The nanosheets used in this study are indirect band gap semiconductors, because their direct band gap values fitted from  $n = 1/2$  were larger than indirect ones. Direct transformation of the UV-vis absorption spectra gives the Tauc plots shown in Figure 3a, where an artificial decrease in band gap due to particle light scattering is observed. For a more accurate determination of the band gap, the spectra were corrected by subtracting a linear baseline, which was made by extrapolating a tangent line to the absorbance in the  $\sim 400$ – $500$  nm region across the spectrum. The resulting corrected plots are shown in Figure 3a. It is worth noting that this

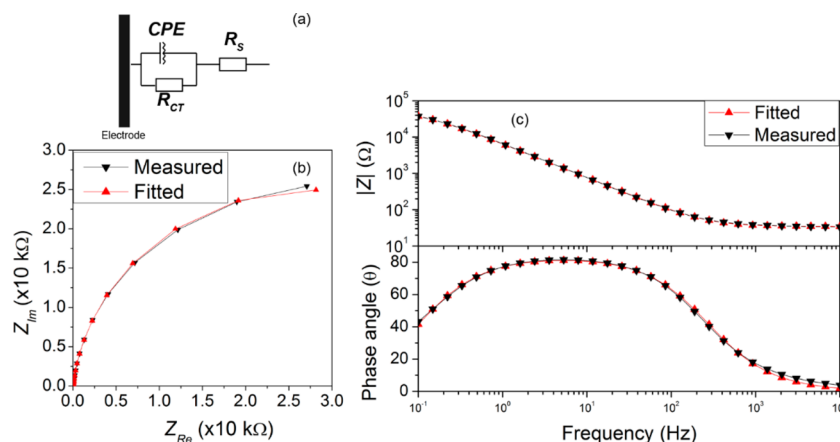


**Figure 4.** (a) Equivalent circuit (Randles circuit) used for fitting of EIS data. Nyquist and (b) and Bode plots (c) of EIS data from five-layer  $\text{Ca}_2\text{Nb}_3\text{O}_{10}$  nanosheet films on FTO at  $-0.7$  V in a pH 7.8 aqueous electrolyte.

method can only partially remove the scattering contribution from the spectra because the scattering efficiency increases as  $1/\lambda^4$ .<sup>45</sup>

Scattering-corrected Tauc plots were constructed for other nanosheet compositions as shown in Figure 3b, and band gap values of  $\text{Sr}_2\text{Nb}_3\text{O}_{10}$ ,  $\text{Ca}_2\text{Nb}_3\text{O}_{10}$ ,  $\text{Ca}_2\text{Nb}_{2.25}\text{Ta}_{0.75}\text{O}_{10}$ , and  $\text{Ca}_2\text{Nb}_{1.5}\text{Ta}_{1.5}\text{O}_{10}$  were estimated to be  $3.77 \pm 0.03$ ,  $3.81 \pm 0.04$ ,  $3.88 \pm 0.03$ , and  $3.97 \pm 0.04$  eV, respectively. The trends we observe are that A-site Sr gives a slightly smaller bandgap than A-site Ca, and that the substitution of Ta for Nb on the B site increases the band gap. These trends are consistent with earlier reports by Maeda et al.,<sup>30,35</sup> although they reported smaller band gaps, possibly because their UV–vis diffuse reflectance measurements were made with restacked nanosheets instead of few-layer nanosheet films.

**Mott–Schottky Experiments.** The flat-band potentials of nanosheets at various pH values were evaluated by electrochemical impedance spectroscopy using the Mott–Schottky method,<sup>32</sup> which is based on eq 3:

$$\frac{1}{C^2} = \frac{2}{\epsilon\epsilon_0 e N_D} \left( V - V_{\text{FB}} - \frac{k_B T}{e} \right) \quad (3)$$

where  $C$  is the interfacial capacitance normalized to the electrode area,  $N_D$  is the donor density,  $V$  is the applied voltage,  $k_B$  is Boltzmann's constant,  $T$  is the absolute temperature,  $e$  is the electronic charge, and  $\epsilon$  and  $\epsilon_0$  are the dielectric constant of the semiconductor and the permittivity of free space, respectively. With an ideal semiconductor–solution interface, a plot of  $1/C^2$  against  $V$  yields a straight line and its intercept on the  $V$  axis corresponds to  $V_{\text{FB}}$ .

Working electrodes were prepared by depositing five layers of PDDA/nanosheets onto FTO glass. In order to ensure good contact between nanosheets, the electrodes were heated to 200 °C and then exposed to UV light for 3 days to remove the solvent and decompose the polycations entrained between the sheets. To evaluate the effectiveness of this process, ten layers of PDDA/nanosheets were deposited on quartz by the LBL technique. We examined XRD patterns of the heat-treated nanosheet films before and after UV exposure (Figure S1, Supporting Information), from which we can see a shift of the basal plane reflections toward higher angle, indicating a decrease in the interlayer distance in the film.

In the frequency range investigated, a Randles circuit was found to model the response of the system adequately (Figure

4):  $R_s$  represents the series resistance from the electrodes, electrolyte, and contacts;  $R_{\text{CT}}$  describes the charge transfer resistance at the electrolyte–electrode interface. A CPE (constant phase element) was used to describe the capacitance behavior of the electrode, which deviates from ideal capacitor due to surface nonhomogeneity.<sup>34</sup> The impedance of a CPE follows eq 4,

$$Z_{\text{CPE}} = \frac{1}{T(j\omega)^n} \quad (4)$$

where  $\omega$  is the applied frequency, and  $T$  ( $0 \leq T \leq 1$ ) and  $n$  are frequency-independent parameters. Although a CPE gave good fits to the data, the parameter  $T$  represents capacitance only when  $n = 1$ . Two models are proposed to determine the effective capacitance from a CPE.<sup>46</sup> Considering that nanosheets spread both laterally and vertically on the substrate, the surface distribution model developed by Brug et al.<sup>47</sup> was used here with the following expression:

$$C_{\text{CPE}} = T^{1/n} \left( \frac{R_s R_{\text{CT}}}{R_s + R_{\text{CT}}} \right)^{(1-n)/n} \quad (5)$$

although a normal-distribution model<sup>48</sup> was found to give very similar results. The capacitance of the CPE was treated only as the space–charge capacitance of the nanosheets and FTO, because the double layer capacitance was considered to be much larger than space–charge capacitance and thus a small contributor to the series capacitance in the Mott–Schottky equation.<sup>33,49</sup>

Mott–Schottky plots of five-layer  $\text{Ca}_2\text{Nb}_3\text{O}_{10}$  nanosheet films and the bare FTO substrate at pH = 7.8 are shown in Figure 5, where three regions of different slopes can be observed. When the applied potential is more positive than  $-0.7$  V (regions 1 and 2), the space–charge region of the nanosheet film is depleted and the capacitance of the working electrode is similar to that of the bare FTO electrode. A linear fit of region 1 gives  $V_{\text{FB}}$  of FTO glass to be about  $-0.5$  V, which is more positive than the value fitted from a bare FTO sample ( $\sim -0.6$  V). The latter is comparable to other reported values when adjusted to an equivalent pH with a pH-dependence of  $-59.2$  mV/pH.<sup>33</sup> As the applied potential approaches values more negative than  $-0.7$  V (region 3), a dramatic increase in the capacitance is observed. Our interpretation of this increase is that the space charge region of the nanosheets begins to

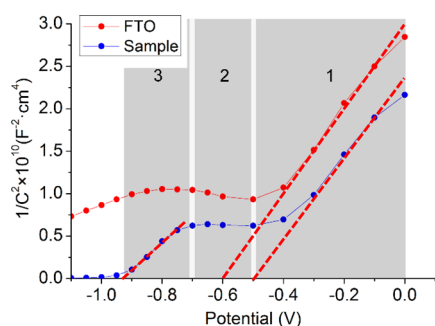


**Figure 5.** Mott–Schottky plots of five-layer  $\text{Ca}_2\text{Nb}_3\text{O}_{10}$  nanosheets and a bare FTO substrate at pH = 7.8. Shaded regions 1, 2, and 3 correspond to potential ranges in which the capacitance is dominated by the FTO substrate, the FTO/nanosheet interface, and the semiconducting nanosheet film.

contribute to the measured capacitance. We can then determine  $V_{\text{FB}}$  of the nanosheets via a linear fit in this region to be  $-0.944 \pm 0.004$  V based on three measurements. A positive slope in region 3 indicates that the  $\text{Ca}_2\text{Nb}_3\text{O}_{10}$  nanosheets are *n*-type, which was also true of the other nanosheets investigated.

Ideally, if the thin semiconducting film is in good contact with the substrate, one should observe only two regions of different slopes, one from the substrate and one from the film.<sup>33,34</sup> The crossing point of the two slopes indicates the potential at which the depletion layer reaches the thin film/substrate interface. However, in our experiments, there is an additional region, region 2 in Figure 5, which can be interpreted as a capacitive contribution due to specific ion adsorption between the FTO surface and the nanosheets. Although decomposition of PDDA was achieved via UV exposure, some ion-exchange capacity still remains and intimate contact between the nanosheets and the FTO substrate is not guaranteed.<sup>50</sup> The adsorption of cations may also explain the positive shift of the measured  $V_{\text{FB}}$  of the nanosheet-covered FTO substrate relative to clean FTO.

On the basis of the Mott–Schottky equation, we can also estimate the thickness of space-charge region,  $L_{\text{sc}}$  from eq 6:

$$L_{\text{sc}} = \left( \frac{2\epsilon\epsilon_0}{eN_{\text{D}}} \right)^{1/2} \left( V - V_{\text{FB}} - \frac{k_{\text{B}}T}{e} \right)^{1/2} \quad (6)$$

Using a dielectric constant of 210,<sup>51</sup> we calculated the space-charge region thickness of the five-layer  $\text{Ca}_2\text{Nb}_3\text{O}_{10}$  nanosheet film to be about 15 nm, which is comparable to the value estimated from AFM data ( $5 \times 1.6 = 9$  nm).

Equation 6 also suggests that the potential width of region 3 scales with the square of the thickness of the nanosheet layer, which, however, is not supported experimentally, because the width of region 3 appears to be independent of the number of layers deposited. We repeated the measurements on gold-coated slides (which have a smoother surface than FTO) and no significant correlation between the width of region 3 and the thickness of the nanosheet film was found (Figure 6). One explanation may be that the measured capacitance arises not only from the nanosheet film but also from the electrical double layer at the electrode surface, especially if the solution can penetrate between the nanosheets.

Nanosheets of other compositions were also characterized by EIS, and their flat-band potentials at different pH values are summarized in Figure 7. The flat-band potentials of all nanosheets show a pH dependence close to  $\sim 59$  mV per pH,

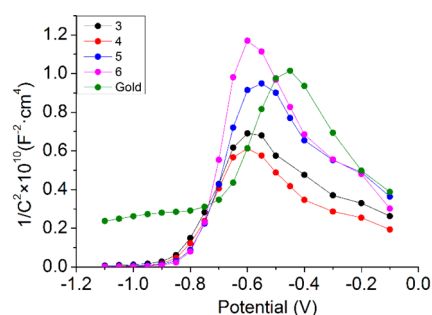


**Figure 6.** Mott–Schottky plots of gold-coated slides with different numbers of  $\text{Ca}_2\text{Nb}_3\text{O}_{10}$  nanosheet layers at pH 6.7.

which can be explained by proton adsorption/desorption at the surface oxide groups of the semiconductor.<sup>52</sup> Consistent with expectations from eq 1, we find that  $\text{Sr}_2\text{Nb}_3\text{O}_{10}$  has a more positive  $V_{\text{FB}}$  value than  $\text{Ca}_2\text{Nb}_3\text{O}_{10}$ , and that the introduction of Ta into Nb sites shifts  $V_{\text{FB}}$  of the nanosheets to more negative values.

To gain more insight into the correlation of composition with electronic properties, we performed DFT calculations of the electronic structure of the nanosheets (Figure 7b; see Figure S2, Figure S3, and Table S2 in Supporting Information for optimized structures, band structures, and work functions, respectively). It is worth noting that although DFT calculations systematically underestimate band gaps even when the hybrid functional HSE06 is adopted, they can provide useful information about trends in energies and about the contributions of atomic orbitals to the energy bands. The calculated variation in band gaps is consistent with our measurements. The partial density of states analysis (Figure S4, Supporting Information) indicates that 2p orbitals from oxygen and 3d orbitals from B-site cations contribute the most to the valence band and conduction bands, respectively. Therefore, substitution on the B site can directly influence the energy of the conduction band edge. A-site cations, although not directly contributing to the frontier orbitals, may alter the electronic structure through changes in A–O bond strength. We observed that the average Mulliken bond order for A–O bonds decreased from 0.06 for  $\text{HCa}_2\text{Nb}_3\text{O}_{10}$  to 0.05 for  $\text{HSr}_2\text{Nb}_3\text{O}_{10}$  in our calculations. The smaller bond order implies a more ionic (less covalent) bond for Sr–O relative to Ca–O, which is consistent with the results of a study of  $\text{ABO}_3$  perovskites by Chen et al.<sup>53</sup>

We also applied Matsumoto’s empirical eq 1 to estimate the conduction band-edge potentials of the nanosheets. In this correlation, the energy difference between the conduction band edge and Fermi level was estimated from the conductivity of the semiconductors. For wide band gap semiconductors such as those in this study ( $>10^4 \Omega\text{-cm}$  resistivity<sup>54</sup>), 0.4 eV was used. The estimated Fermi level potentials of the nanosheets are plotted in Figure 7a (assuming a pH dependence of  $-59$  mV/pH), from which we can see that the empirical equation gives reasonably good predictions.

When extending the EIS measurements to other layered metal oxide nanosheets including  $\text{Sr}_2\text{Ta}_3\text{O}_{10}$ ,  $\text{Ca}_2\text{Ta}_3\text{O}_{10}$ ,  $\text{TiO}_x$ , and  $\text{TiNbO}_5$ , we found two problems in obtaining useful Mott–Schottky plots. First, tantalate compounds are expected to possess a very negative  $V_{\text{FB}}$  ( $<-1.2$  V in neutral solution), and EIS measurements in this potential range require the inclusion of a Warburg element in an equivalent circuit to account for diffusion-controlled phenomena, which complicates

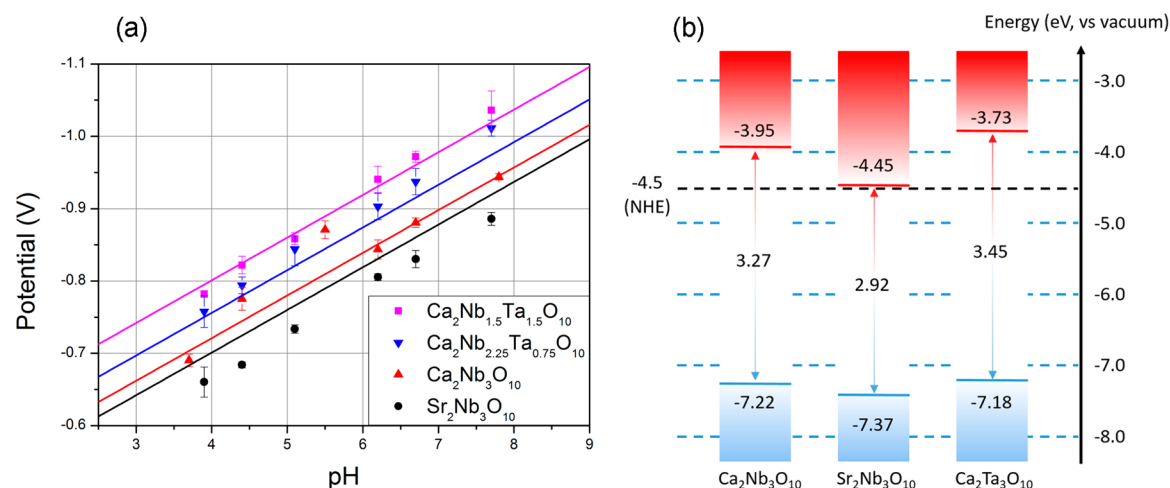


**Figure 7.** (a) Flat-band potentials of different nanosheet films at various pHs on FTO substrates. Dots are the measured data; solid lines are estimated Fermi level potentials based on eq 1. (b) DFT-calculated energy diagram including conduction band minimum, valence band maximum, and band gap values for  $\text{HCa}_2\text{Nb}_3\text{O}_{10}$ ,  $\text{HSr}_2\text{Nb}_3\text{O}_{10}$ , and  $\text{HCa}_2\text{Ta}_3\text{O}_{10}$  nanosheets.

the determination of the nanosheet capacitance. Second, for  $\text{TiO}_x$  and  $\text{TiNbO}_5$  nanosheets, the Randles circuit did not give good fits to the EIS spectra collected at all scanned potentials. We found that as the potential approached the expected value of  $V_{\text{FB}}$ , the measured EIS spectra deviated from the Randles circuit fit (Figure S5, Supporting Information). We suspect that electrochemical reduction of  $\text{TiO}_x$  and  $\text{TiNbO}_5$  nanosheets at negative potentials may complicate the analysis in these cases.

## CONCLUSIONS

Molecularly thin perovskite nanosheets  $\text{A}_2\text{B}_3\text{O}_{10}$  with different atomic compositions, including  $\text{Sr}_2\text{Nb}_3\text{O}_{10}$ ,  $\text{Ca}_2\text{Nb}_3\text{O}_{10}$ ,  $\text{Ca}_2\text{Nb}_{2.25}\text{Ta}_{0.75}\text{O}_{10}$ , and  $\text{Ca}_2\text{Nb}_{1.5}\text{Ta}_{1.5}\text{O}_{10}$ , were grown as multilayer films on different substrates by LBL adsorption of polycations and nanosheets. The band gaps of these nanosheets could be determined by constructing scattering-corrected Tauc plots. Mott–Schottky analysis of electrochemical impedance measurements indicated that all nanosheets in this family were n type semiconductors and had a pH dependence of their flat-band potentials close to  $-59$  mV per pH. DFT calculations indicated that the electronic structure can be affected by the strength of A–O bonding and by substitution of Ta for Nb on B-sites. As long as the materials are robust and the equivalent circuit is consistent throughout the whole measurement, one can use the Mott–Schottky analysis to measure the flat-band potentials of the exfoliated metal oxide nanosheets in contact with aqueous solutions. The results of these measurements support Matsumoto’s empirical correlation of conduction band-edge positions with band gaps for metal oxide semiconductors.

## ASSOCIATED CONTENT

### Supporting Information

The Supporting Information is available free of charge on the ACS Publications website at DOI: 10.1021/acsami.6b02901.

EDS data of nanosheets, XRD patterns before and after UV photolysis of multilayer films, results of DFT calculations, and EIS spectra of  $\text{TiO}_x$  nanosheet films (PDF)

## AUTHOR INFORMATION

### Corresponding Author

\*E-mail: tem5@psu.edu.

### Notes

The authors declare no competing financial interest.

## ACKNOWLEDGMENTS

This work was supported by the Office of Basic Energy Sciences, Division of Chemical Sciences, Geosciences, and Energy Biosciences, Department of Energy, under contract DE-FG02-07ER15911.

## REFERENCES

- Ma, R.; Sasaki, T. Two-Dimensional Oxide and Hydroxide Nanosheets: Controllable High-Quality Exfoliation, Molecular Assembly, and Exploration of Functionality. *Acc. Chem. Res.* **2015**, *48* (1), 136–143.
- Osada, M.; Sasaki, T. Exfoliated Oxide Nanosheets: New Solution to Nanoelectronics. *J. Mater. Chem.* **2009**, *19* (17), 2503–2511.
- Osterloh, F. E. Inorganic Materials as Catalysts for Photoelectrochemical Splitting of Water. *Chem. Mater.* **2008**, *20* (1), 35–54.
- Domen, K.; Kudo, A.; Shibata, M.; Tanaka, A.; Maruya, K.-I.; Onishi, T. Novel Photocatalysts, Ion-exchanged  $\text{K}_4\text{Nb}_6\text{O}_{17}$ , with a Layer Structure. *J. Chem. Soc., Chem. Commun.* **1986**, *23*, 1706–1707.
- Sayama, K.; Tanaka, A.; Domen, K.; Maruya, K.; Onishi, T. Photocatalytic Decomposition of Water over Platinum-Intercalated  $\text{K}_4\text{Nb}_6\text{O}_{17}$ . *J. Phys. Chem.* **1991**, *95* (3), 1345–1348.
- Kim, Y. I.; Salim, S.; Huq, M. J.; Mallouk, T. E. Visible Light Photolysis of Hydrogen Iodide Using Sensitized Layered Semiconductor Particles. *J. Am. Chem. Soc.* **1991**, *113* (25), 9561–9563.
- Kim, Y. I.; Atherton, S. J.; Brigham, E. S.; Mallouk, T. E. Sensitized Layered Metal Oxide Semiconductor Particles for Photochemical Hydrogen Evolution from Non-sacrificial Electron Donors. *J. Phys. Chem.* **1993**, *97* (45), 11802–11810.
- Saupe, G. B.; Kim, W.; Schmehl, R. H.; Mallouk, T. E. Visible Light Photolysis of Hydrogen Iodide Using Sensitized Layered Metal Oxide Semiconductors: The Role of Surface Chemical Modification in Controlling Back Electron Transfer Reactions. *J. Phys. Chem. B* **1997**, *101* (14), 2508–2513.
- Keller, S. W.; Kim, H. N.; Mallouk, T. E. Layer-by-Layer Assembly of Intercalation Compounds and Heterostructures on Surfaces: Towards Molecular “Beaker” Epitaxy. *J. Am. Chem. Soc.* **1994**, *116* (19), 8817–8818.

- (10) Kleinfeld, E. R.; Ferguson, G. S. Stepwise formation of Multilayered Nanostructural Films From Macromolecular Precursors. *Science* **1994**, *265* (5170), 370–373.
- (11) Saupe, G. B.; Waraksa, C. C.; Kim, H.-H.; Han, Y. J.; Kaschak, D. M.; Skinner, D. M.; Mallouk, T. E. Nanoscale Tubules Formed by Exfoliation of Potassium Hexaniobate. *Chem. Mater.* **2000**, *12* (6), 1556–1562.
- (12) Ma, R.; Bando, Y.; Sasaki, T. Directly Rolling Nanosheets into Nanotubes. *J. Phys. Chem. B* **2004**, *108* (7), 2115–2119.
- (13) Keller, S. W.; Johnson, S. A.; Brigham, E. S.; Yonemoto, E. H.; Mallouk, T. E. Photoinduced Charge Separation in Multilayer Thin Films Grown by Sequential Adsorption of Polyelectrolytes. *J. Am. Chem. Soc.* **1995**, *117* (51), 12879–12880.
- (14) Kaschak, D. M.; Lean, J. T.; Waraksa, C. C.; Saupe, G. B.; Usami, H.; Mallouk, T. E. Photoinduced Energy and Electron Transfer Reactions in Lamellar Polyanion/Polycation Thin Films: Toward an Inorganic “Leaf”. *J. Am. Chem. Soc.* **1999**, *121* (14), 3435–3445.
- (15) Maeda, K.; Eguchi, M.; Youngblood, W. J.; Mallouk, T. E. Niobium Oxide Nanoscrolls as Building Blocks for Dye-Sensitized Hydrogen Production from Water under Visible Light Irradiation. *Chem. Mater.* **2008**, *20* (21), 6770–6778.
- (16) Maeda, K.; Eguchi, M.; Youngblood, W. J.; Mallouk, T. E. Calcium Niobate Nanosheets Prepared by the Polymerized Complex Method as Catalytic Materials for Photochemical Hydrogen Evolution. *Chem. Mater.* **2009**, *21* (15), 3611–3617.
- (17) Maeda, K.; Mallouk, T. E. Comparison of Two- and Three-Layer Restacked Dion–Jacobson Phase Niobate Nanosheets as Catalysts for Photochemical Hydrogen Evolution. *J. Mater. Chem.* **2009**, *19* (27), 4813–4818.
- (18) Sabio, E. M.; Chamousis, R. L.; Browning, N. D.; Osterloh, F. E. Photocatalytic Water Splitting with Suspended Calcium Niobium Oxides: Why Nanoscale Is Better Than Bulk – A Kinetic Analysis. *J. Phys. Chem. C* **2012**, *116* (4), 3161–3170.
- (19) Abe, R.; Shinmei, K.; Koumura, N.; Hara, K.; Ohtani, B. Visible-Light-Induced Water Splitting Based on Two-Step Photoexcitation between Dye-Sensitized Layered Niobate and Tungsten Oxide Photocatalysts in the Presence of a Triiodide/Iodide Shuttle Redox Mediator. *J. Am. Chem. Soc.* **2013**, *135* (45), 16872–16884.
- (20) Oshima, T.; Lu, D.; Ishitani, O.; Maeda, K. Intercalation of Highly Dispersed Metal Nanoclusters into a Layered Metal Oxide for Photocatalytic Overall Water Splitting. *Angew. Chem., Int. Ed.* **2015**, *54* (9), 2698–2702.
- (21) Osterloh, F. Nanoscale Effects in Water Splitting Photocatalysis. *Topics in Current Chemistry*; Solar Energy for Fuels; Springer: New York, 2015; Vol. 371, pp 105–142.
- (22) Nozik, A. J.; Memming, R. Physical Chemistry of Semiconductor–Liquid Interfaces. *J. Phys. Chem.* **1996**, *100* (31), 13061–13078.
- (23) Chen, Z.; Dinh, H. N.; Miller, E. *Photoelectrochemical Water Splitting*; Springer Briefs in Energy; Springer: New York, 2013.
- (24) Sakai, N.; Ebina, Y.; Takada, K.; Sasaki, T. Electronic Band Structure of Titania Semiconductor Nanosheets Revealed by Electrochemical and Photoelectrochemical Studies. *J. Am. Chem. Soc.* **2004**, *126* (18), 5851–5858.
- (25) Akatsuka, K.; Takanashi, G.; Ebina, Y.; Haga, M.; Sasaki, T. Electronic Band Structure of Exfoliated Titanium- And/or Niobium-Based Oxide Nanosheets Probed by Electrochemical and Photoelectrochemical Measurements. *J. Phys. Chem. C* **2012**, *116* (23), 12426–12433.
- (26) Redmond, G.; Fitzmaurice, D. Spectroscopic Determination of Flatband Potentials for Polycrystalline Titania Electrodes in Non-aqueous Solvents. *J. Phys. Chem.* **1993**, *97* (7), 1426–1430.
- (27) Chamousis, R. L.; Osterloh, F. E. Use of Potential Determining Ions to Control Energetics and Photochemical Charge Transfer of a Nanoscale Water Splitting Photocatalyst. *Energy Environ. Sci.* **2014**, *7* (2), 736–743.
- (28) Butler, M. A. Prediction of Flatband Potentials at Semiconductor–Electrolyte Interfaces from Atomic Electronegativities. *J. Electrochem. Soc.* **1978**, *125* (2), 228–232.
- (29) Matsumoto, Y. Energy Positions of Oxide Semiconductors and Photocatalysis with Iron Complex Oxides. *J. Solid State Chem.* **1996**, *126* (2), 227–234.
- (30) Maeda, K.; Sahara, G.; Eguchi, M.; Ishitani, O. Hybrids of a Ruthenium(II) Polypyridyl Complex and a Metal Oxide Nanosheet for Dye-Sensitized Hydrogen Evolution with Visible Light: Effects of the Energy Structure on Photocatalytic Activity. *ACS Catal.* **2015**, *5* (3), 1700–1707.
- (31) Maeda, K.; Eguchi, M.; Lee, S. H. A.; Youngblood, W. J.; Hata, H.; Mallouk, T. E. Photocatalytic Hydrogen Evolution from Hexaniobate Nanoscrolls and Calcium Niobate Nanosheets Sensitized by Ruthenium(II) Bipyridyl Complexes. *J. Phys. Chem. C* **2009**, *113* (18), 7962–7969.
- (32) Gelderman, K.; Lee, L.; Donne, S. W. Flat-Band Potential of a Semiconductor: Using the Mott–Schottky Equation. *J. Chem. Educ.* **2007**, *84* (4), 685–688.
- (33) Kavan, L.; Tétreault, N.; Moehl, T.; Grätzel, M. Electrochemical Characterization of TiO<sub>2</sub> Blocking Layers for Dye-Sensitized Solar Cells. *J. Phys. Chem. C* **2014**, *118* (3), 16408–16418.
- (34) van de Krol, R.; Goossens, A.; Schoonman, J. Mott–Schottky Analysis of Nanometer-Scale Thin-Film Anatase TiO<sub>2</sub>. *J. Electrochem. Soc.* **1997**, *144* (5), 1723–1727.
- (35) Maeda, K.; Eguchi, M.; Oshima, T. Perovskite Oxide Nanosheets with Tunable Band-Edge Potentials and High Photocatalytic Hydrogen-Evolution Activity. *Angew. Chem., Int. Ed.* **2014**, *53* (48), 13164–13168.
- (36) Thangadurai, V.; Schmid-Beurmann, P.; Weppner, W. Synthesis, Structure, and Electrical Conductivity of A′[A<sub>2</sub>B<sub>3</sub>O<sub>10</sub>](A′ = Rb, Cs; A = Sr, Ba; B = Nb, Ta): New Members of Dion–Jacobson-Type Layered Perovskites. *J. Solid State Chem.* **2001**, *158* (2), 279–289.
- (37) Xu, F. F.; Ebina, Y.; Bando, Y.; Sasaki, T. Structural Characterization of (TBA, H)Ca<sub>2</sub>Nb<sub>3</sub>O<sub>10</sub> Nanosheets Formed by Delamination of a Precursor-Layered Perovskite. *J. Phys. Chem. B* **2003**, *107* (36), 9638–9645.
- (38) Clark, S. J.; Segall, M. D.; Pickard, C. J.; Hasnip, P. J.; Probert, M. I. J.; Refson, K.; Payne, M. C. First Principles Methods Using CASTEP. *Z. Kristallogr. - Cryst. Mater.* **2005**, *220* (5–6), 567–570.
- (39) Strayer, M. E.; Senftle, T. P.; Winterstein, J. P.; Vargas-Barbosa, N. M.; Sharma, R.; Rioux, R. M.; Janik, M. J.; Mallouk, T. E. Charge Transfer Stabilization of Late Transition Metal Oxide Nanoparticles on a Layered Niobate Support. *J. Am. Chem. Soc.* **2015**, *137* (51), 16216–16224.
- (40) Perdew, J. P.; Burke, K.; Ernzerhof, M. Generalized Gradient Approximation Made Simple. *Phys. Rev. Lett.* **1996**, *77* (18), 3865–3868.
- (41) Segall, M. D.; Shah, R.; Pickard, C. J.; Payne, M. C. Population Analysis of Plane-Wave Electronic Structure Calculations of Bulk Materials. *Phys. Rev. B: Condens. Matter Mater. Phys.* **1996**, *54* (23), 16317–16320.
- (42) Krukau, A. V.; Vydrov, O. A.; Izmaylov, A. F.; Scuseria, G. E. Influence of the Exchange Screening Parameter on the Performance of Screened Hybrid Functionals. *J. Chem. Phys.* **2006**, *125* (22), 224106.
- (43) Schaak, R. E.; Mallouk, T. E. Perovskites by Design: A Toolbox of Solid-State Reactions. *Chem. Mater.* **2002**, *14* (4), 1455–1471.
- (44) Decher, G. Fuzzy Nanoassemblies: Toward Layered Polymeric Multicomposites. *Science* **1997**, *277* (5330), 1232–1237.
- (45) Bohren, C. F.; Huffman, D. R. *Absorption and Scattering of Light by Small Particles*; Bohren, C. F., Huffman, D. R., Eds.; Wiley: Weinheim, Germany, 1983.
- (46) Hirschorn, B.; Orazem, M. E.; Tribollet, B.; Vivier, V.; Frateur, I.; Musiani, M. Determination of Effective Capacitance and Film Thickness from Constant-Phase-Element Parameters. *Electrochim. Acta* **2010**, *55* (21), 6218–6227.
- (47) Brug, G. J.; van den Eeden, A. L. G.; Sluyters-Rehbach, M.; Sluyters, J. H. The Analysis of Electrode Impedances Complicated by the Presence of a Constant Phase Element. *J. Electroanal. Chem. Interfacial Electrochem.* **1984**, *176* (1–2), 275–295.

(48) Hsu, C. H.; Mansfeld, F. Concerning the Conversion of the Constant Phase Element Parameter  $Y_0$  into a Capacitance. *Corrosion* **2001**, *57* (9), 747–748.

(49) De Gryse, R. On the Interpretation of Mott-Schottky Plots Determined at Semiconductor/Electrolyte Systems. *J. Electrochem. Soc.* **1975**, *122* (5), 711–712.

(50) Sasaki, T.; Ebina, Y.; Fukuda, K.; Tanaka, T.; Harada, M.; Watanabe, M. Titania Nanostructured Films Derived from a Titania Nanosheet/Polycation Multilayer Assembly via Heat Treatment and UV Irradiation. *Chem. Mater.* **2002**, *14* (8), 3524–3530.

(51) Osada, M.; Akatsuka, K.; Ebina, Y.; Funakubo, H.; Ono, K.; Takada, K.; Sasaki, T. Robust High- $\kappa$  Response in Molecularly Thin Perovskite Nanosheets. *ACS Nano* **2010**, *4* (9), 5225–5232.

(52) Matsumoto, Y. Dependence of the Band Bending of the Oxide Semiconductors on pH. *J. Electrochem. Soc.* **1989**, *136* (5), 1389–1391.

(53) Chen, Z.-X.; Chen, Y.; Jiang, Y.-S. Comparative Study of ABO<sub>3</sub> Perovskite Compounds. I. ATiO<sub>3</sub> (A = Ca, Sr, Ba, and Pb) Perovskites. *J. Phys. Chem. B* **2002**, *106* (39), 9986–9992.

(54) Draskovic, T. I.; Wang, T.; Henderson, C. N.; Mallouk, T. E. Protonic and Electronic Conductivity of the Layered Perovskite Oxides HCa<sub>2</sub>Nb<sub>3</sub>O<sub>10</sub> and Ca<sub>4</sub>Nb<sub>6</sub>O<sub>19</sub>. *Int. J. Hydrogen Energy* **2014**, *39* (9), 4576–4580.